

the BS to the user. We assume that each RIS is composed of L^2 reflecting elements with isotropic electromagnetic properties, which is arranged in an $L \times L$ uniform rectangular array (URA). Without loss of generality, we assume L is an even number, and thus the index of the central element is given by $(1 + \frac{L-1}{2}, 1 + \frac{L-1}{2})$. The vertical and horizontal spacing between two adjacent elements is $\Delta\lambda$, where Δ is the scaling factor with respect to (w.r.t.) the signal carrier wavelength λ .

A. Cascaded Channel Model

The geometric channel model [9] is adopted for the individual BS-RIS and RIS-user links, which is based on the angle-of-departures (AoDs), angle-of-arrivals (AoAs), and the complex path gains of each path. In this letter, we assume that the channel state information (CSI), including all the angles and other channel coefficients, are perfectly known at the BS. The CSI acquisition methods are studied in [10] by inserting active elements that are connected to the baseband processing unit into the RISs. The multi-path channel $\mathbf{G}_n \in \mathbb{C}^{L^2 \times M}$ from the BS to the n -th RIS can be expressed as

$$\mathbf{G}_n = \sum_{d=1}^{D_n} \alpha_{n,d} \mathbf{a}(\vartheta_{n,d}^{\text{RIS}}, \psi_{n,d}^{\text{RIS}}) \mathbf{b}^H(\phi_{n,d}^{\text{BS}}), \quad (1)$$

where D_n denotes the number of resolvable paths; $\alpha_{n,d}$ denotes the complex path gain of the d -th path; $\vartheta_{n,d}^{\text{RIS}}$ and $\psi_{n,d}^{\text{RIS}}$ denote the corresponding elevation and azimuth AoAs, respectively; and $\phi_{n,d}^{\text{BS}}$ denotes the corresponding AoD. The steering vector $\mathbf{a}(\vartheta_{n,d}^{\text{RIS}}, \psi_{n,d}^{\text{RIS}}) \in \mathbb{C}^{L^2 \times 1}$ is defined as

$$\mathbf{a}(\vartheta_{n,d}^{\text{RIS}}, \psi_{n,d}^{\text{RIS}}) = \mathbf{a}^x(\vartheta_{n,d}^{\text{RIS}}, \psi_{n,d}^{\text{RIS}}) \otimes \mathbf{a}^y(\vartheta_{n,d}^{\text{RIS}}, \psi_{n,d}^{\text{RIS}}), \quad (2)$$

where \otimes denotes the Kronecker product; $\mathbf{a}^x(\vartheta_{n,d}^{\text{RIS}}, \psi_{n,d}^{\text{RIS}}) \in \mathbb{C}^{L \times 1}$ and $\mathbf{a}^y(\vartheta_{n,d}^{\text{RIS}}, \psi_{n,d}^{\text{RIS}}) \in \mathbb{C}^{L \times 1}$ are given as follows:

$$\begin{aligned} [\mathbf{a}^x(\vartheta_{n,d}^{\text{RIS}}, \psi_{n,d}^{\text{RIS}})]_\ell &= \frac{1}{\sqrt{L}} e^{j\pi\Delta(L-1)\sin(\vartheta_{n,d}^{\text{RIS}})\cos(\psi_{n,d}^{\text{RIS}})} \\ &\times e^{-j2\pi\Delta(\ell-1)\sin(\vartheta_{n,d}^{\text{RIS}})\cos(\psi_{n,d}^{\text{RIS}})}, \quad \ell \in [L]; \end{aligned} \quad (3)$$

$$\begin{aligned} [\mathbf{a}^y(\vartheta_{n,d}^{\text{RIS}}, \psi_{n,d}^{\text{RIS}})]_\ell &= \frac{1}{\sqrt{L}} e^{j\pi\Delta(L-1)\sin(\vartheta_{n,d}^{\text{RIS}})\sin(\psi_{n,d}^{\text{RIS}})} \\ &\times e^{-j2\pi\Delta(\ell-1)\sin(\vartheta_{n,d}^{\text{RIS}})\sin(\psi_{n,d}^{\text{RIS}})}, \quad \ell \in [L], \end{aligned} \quad (4)$$

where j denotes the imaginary unit. The steering vector $\mathbf{b}(\phi_{n,d}^{\text{BS}}) \in \mathbb{C}^{M \times 1}$ is given by

$$\begin{aligned} [\mathbf{b}(\phi_{n,d}^{\text{BS}})]_m &= \frac{1}{\sqrt{M}} e^{j\frac{\pi(M-1)}{2}\sin(\phi_{n,d}^{\text{BS}})} \\ &\times e^{-j\pi(m-1)\sin(\phi_{n,d}^{\text{BS}})}, \quad m \in [M]. \end{aligned} \quad (5)$$

Similarly, the multi-path channel $\mathbf{f}_n^H \in \mathbb{C}^{1 \times L^2}$ from the n -th RIS to the user is modeled as

$$\mathbf{f}_n^H = \sum_{k=1}^{K_n} \beta_{n,k} \mathbf{u}^H(\theta_{n,k}^{\text{RIS}}, \phi_{n,k}^{\text{RIS}}), \quad (6)$$

where K_n denotes the number of resolvable paths; $\beta_{n,k}$ denotes the complex path gain of the k -th path; $\theta_{n,k}^{\text{RIS}}$ and $\phi_{n,k}^{\text{RIS}}$ denote the corresponding elevation and azimuth AoDs;

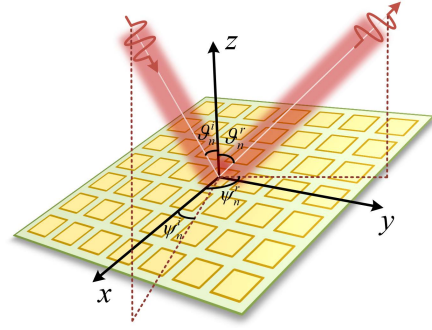


Fig. 2. An illustration of the reflection property of a RIS.

the steering vector $\mathbf{u}(\theta_{n,k}^{\text{RIS}}, \phi_{n,k}^{\text{RIS}}) \in \mathbb{C}^{L^2 \times 1}$ is defined in the same manner as $\mathbf{a}(\vartheta_{n,d}^{\text{RIS}}, \psi_{n,d}^{\text{RIS}})$ in (2).

By ignoring the direct link from the BS to the user, the received signal at the user can be expressed as

$$y = \sum_{n=1}^N \mathbf{f}_n^H \Theta_n \mathbf{G}_n \mathbf{w} s + n = \mathbf{h}^H \mathbf{w} s + n, \quad (7)$$

where $\Theta_n = \text{diag}(e^{j\theta_{n,1}}, \dots, e^{j\theta_{n,L^2}})$ denotes the diagonal phase shifts matrix for the n -th RIS, with reflecting amplitude being 1; \mathbf{w} denotes the transmit beamforming vector at the BS; s denotes the transmit data symbol; n denotes additive white Gaussian noise (AWGN) with zero mean and variance σ^2 ; and $\mathbf{h}^H = \sum_{n=1}^N \mathbf{f}_n^H \Theta_n \mathbf{G}_n$ denotes the cascaded BS-RIS-user channel.

B. Reflection-Angle-Based Cascaded Channel Representation

To reconfigure the wireless propagation environment, passive beamforming (PB) design problems have been widely studied in [1], [2], [5]–[7] and the references therein. However, the aforementioned work considers that the phase shift of each RIS element is independently adjusted, where a total of NL^2 variables should be jointly optimized. The complexity of solving such non-convex PB problems is sensitive to the size of the variable space and is in general very high. For example, the involved complexity is $\mathcal{O}((NL^2)^6)$ via the semi-definite relaxation (SDR) method [2], which is prohibitively high especially for large surfaces consisting of thousands of reflecting elements. To meet the requirement of dense deployment of large RISs, we turn to explore the reflection property of each RIS, so as to significantly reduce the dimension of the PB variable space and thus simplify the optimization design.

According to the generalized Snell's law [8], to realize the electromagnetic wave deflection from the incident elevation/azimuth angles $(\vartheta_n^i, \psi_n^i)$ to the reflection elevation/azimuth angles $(\vartheta_n^r, \psi_n^r)$ in Fig. 2, the phase shifts function of each RIS is affine along both the x - and y -axes¹. More

¹The generalized Snell's law is derived from infinite-size and continuous surface to guarantee specular reflection. However, it is reported in [11] that the beamwidth of the reflected wave from a $10\lambda \times 10\lambda$ RIS is about 10° , which indicates that a finite-size RIS with discrete elements is far from a specular reflector. While in this case, following the generalized Snell's law still guarantees that the main lobe of the beam is aligned with the target user.

specifically, the phase shift of the (i, j) -th element of the n -th RIS satisfies [12]

$$\begin{aligned} \theta_{n,(i-1)L+j} &= 2\pi\Delta \left(i-1 - \frac{L-1}{2} \right) q_n^x \\ &\quad + 2\pi\Delta \left(j-1 - \frac{L-1}{2} \right) q_n^y + \varphi_n, \end{aligned} \quad (8)$$

where the design parameters include: 1) q_n^x and q_n^y , denoting respectively the phase gradients of the x - and y -axes, which control the reflection angle by altering the phase difference between two adjacent elements; and 2) φ_n , denoting the common phase offset of the n -th RIS, which aligns the phase of the reflected beam. In order to steer the impinging signal from $(\vartheta_n^i, \psi_n^i)$ to $(\vartheta_n^r, \psi_n^r)$, the phase gradient $\mathbf{q}_n = [q_n^x, q_n^y]$ should be set as

$$q_n^x = \sin \vartheta_n^r \cos \psi_n^r + \sin \vartheta_n^i \cos \psi_n^i; \quad (9)$$

$$q_n^y = \sin \vartheta_n^r \sin \psi_n^r + \sin \vartheta_n^i \sin \psi_n^i. \quad (10)$$

Since the absolute values of both $\sin(\cdot)$ and $\cos(\cdot)$ are no larger than 1, $q_n^x, q_n^y \in [-2, 2]$ always holds for any incident and reflection angles. Moreover, due to the 2π -periodicity of the phase shift, q_n^x and $q_n^x + \frac{1}{\Delta}$ (q_n^y and $q_n^y + \frac{1}{\Delta}$) yield the same RIS response function. Therefore, we have $q_n^x, q_n^y \in [-\bar{q}, \bar{q}]$, where $\bar{q} = \min \left\{ 2, \frac{1}{2\Delta} \right\}$.

It is worth mentioning that the structured phase shifts in (8) fully realize the reflection capability of a RIS. Furthermore, for URA-shaped RISs, the variable space reduces from NL^2 to $3N$, where only q_n^x, q_n^y and φ_n need to be customized for the n -th RIS. Motivated by all above, we adopt the phase shifts structure specified in (8) for PB design. Plugging (8) into the cascaded channel \mathbf{h}^H , we have²

$$\begin{aligned} \mathbf{h}^H &= \sum_{n=1}^N \left(\sum_{k=1}^{K_n} \beta_{n,k} \mathbf{u}_{n,k}^H \right) \Theta_n \left(\sum_{d=1}^{D_n} \alpha_{n,d} \mathbf{a}_{n,d} \mathbf{b}_{n,d}^H \right) \\ &= \sum_{n=1}^N \sum_{k=1}^{K_n} \sum_{d=1}^{D_n} \alpha_{n,d} \beta_{n,k} p_{n,k,d} \mathbf{b}_{n,d}^H, \end{aligned} \quad (11)$$

where

$$\begin{aligned} p_{n,k,d} &= \left(\mathbf{u}_{n,k}^x \otimes \mathbf{u}_{n,k}^y \right)^H \Theta_n \left(\mathbf{a}_{n,d}^x \otimes \mathbf{a}_{n,d}^y \right) \\ &= \sum_{i=1}^L \sum_{j=1}^L [\mathbf{u}_{n,k}^x]_i^* [\mathbf{u}_{n,k}^y]_j^* \theta_{n,(i-1)L+j} [\mathbf{a}_{n,d}^x]_i [\mathbf{a}_{n,d}^y]_j \\ &= \frac{e^{j\varphi_n}}{L^2} \left(e^{j\pi\Delta(L-1)s_{n,k,d}^x} \sum_{i=1}^L e^{-j2\pi\Delta(i-1)s_{n,k,d}^x} \right) \\ &\quad \times \left(e^{j\pi\Delta(L-1)s_{n,k,d}^y} \sum_{j=1}^L e^{-j2\pi\Delta(j-1)s_{n,k,d}^y} \right), \end{aligned} \quad (12)$$

with

$$s_{n,k,d}^x = \sin \theta_{n,k}^{\text{RIS}} \cos \phi_{n,k}^{\text{RIS}} + \sin \vartheta_{n,d}^{\text{RIS}} \cos \psi_{n,d}^{\text{RIS}} - q_n^x; \quad (13)$$

$$s_{n,k,d}^y = \sin \theta_{n,k}^{\text{RIS}} \sin \phi_{n,k}^{\text{RIS}} + \sin \vartheta_{n,d}^{\text{RIS}} \sin \psi_{n,d}^{\text{RIS}} - q_n^y. \quad (14)$$

²The steering vectors $\mathbf{u}(\theta_{n,k}^{\text{RIS}}, \phi_{n,k}^{\text{RIS}})$, $\mathbf{a}(\vartheta_{n,d}^{\text{RIS}}, \psi_{n,d}^{\text{RIS}})$, and $\mathbf{b}(\phi_{n,d}^{\text{BS}})$ are abbreviated to $\mathbf{u}_{n,k}$, $\mathbf{a}_{n,d}$, and $\mathbf{b}_{n,d}$ in the sequel of this paper.

By applying the sum of the geometric progression [13], $p_{n,k,d}$ in (12) can be further expressed as

$$p_{n,k,d} = e^{j\varphi_n} \frac{\text{sinc} \left(\frac{\Delta L s_{n,k,d}^x}{2} \right) \text{sinc} \left(\frac{\Delta L s_{n,k,d}^y}{2} \right)}{\text{sinc} \left(\Delta s_{n,k,d}^x \right) \text{sinc} \left(\Delta s_{n,k,d}^y \right)}, \quad (15)$$

As expected, (15) shows the beam pattern of a finite-size RIS reflector, where the reflection angle should be fine-tuned by adjusting \mathbf{q}_n . We rewrite (11) in a more compact form as

$$\mathbf{h}^H = \mathbf{v}^H \mathbf{H}, \quad (16)$$

where $\mathbf{v} = [e^{j\varphi_1}, \dots, e^{j\varphi_N}]^H$, $\mathbf{H} = [\mathbf{r}_1^H \mathbf{B}_1, \dots, \mathbf{r}_N^H \mathbf{B}_N]$, $\mathbf{B}_n = [\mathbf{b}_{n,1}, \dots, \mathbf{b}_{n,D_n}]^H$, $\mathbf{r}_n = [r_{n,1}, \dots, r_{n,D_n}]^H$, and $r_{n,d} = \alpha_{n,d} \sum_{k=1}^{K_n} \beta_{n,k} |p_{n,k,d}|$.

It is observed that the phase shift expression in (8) is divided into two separate parts in (16), i.e., $\mathbf{Q} = [\mathbf{q}_1, \dots, \mathbf{q}_N]$ inside \mathbf{H} and \mathbf{v} outside \mathbf{H} . The wireless channel thus can be reconfigured from two aspects. Firstly, from the element level, the reflection angle of each RIS can be controlled by adjusting the phase difference, i.e., \mathbf{Q} , between two adjacent elements, which can be regarded as a microscopic PB design. Secondly, from the RIS level, the common phase offset of each RIS, i.e., φ_n , is adjusted to align the phase of each reflected beam arrived at the user, which can be regarded as a macroscopic PB design. This leads to a reflection-angle-based HPB problem, as formally stated in the following section.

III. PROBLEM STATEMENT

We aim to maximize the achievable rate of the user subject to the maximum transmit power constraint at the BS. In the single-user setup in this letter, the objective reduces to the maximization of the received signal power. Thus, the problem can be formulated as

$$\max_{\mathbf{w}, \mathbf{Q}, \mathbf{v}} \quad \|\mathbf{v}^H \mathbf{H} \mathbf{w}\|^2 \quad (17a)$$

$$\text{s. t.} \quad \|\mathbf{w}\|^2 \leq p, \quad (17b)$$

$$|v_n| = 1, \quad \forall n, \quad (17c)$$

$$q_n^x, q_n^y \in [-\bar{q}, \bar{q}], \quad \forall n, \quad (17d)$$

where \mathbf{Q} and \mathbf{v} are the HPB variables. Maximum-ratio transmission (MRT) is applied to obtain the optimal transmit beamforming solution, i.e., $\mathbf{w}^* = \sqrt{p} \frac{\mathbf{H}^H \mathbf{v}}{\|\mathbf{H}^H \mathbf{v}\|}$. By substituting \mathbf{w}^* into the above problem, it can be simplified to the following equivalent problem:

$$\max_{\mathbf{Q}, \mathbf{v}} \quad f(\mathbf{Q}, \mathbf{v}) \triangleq \|\mathbf{v}^H \mathbf{H}\|^2 \quad \text{s. t.} \quad (17c), (17d). \quad (18)$$

IV. HIERARCHICAL PASSIVE BEAMFORMING DESIGN

In this section, we first present an alternating optimization (AO) based algorithm, i.e., HPB-AO algorithm, to optimize the HPB variables in (18). Then, to avoid recursively optimizing \mathbf{Q} and \mathbf{v} , a heuristic algorithm is proposed to split the HPB design into two stages.

Algorithm 1: SA Algorithm

Input: Initial temperature T_{\max} ; terminate temperature T_{\min} ; annealing parameter γ .
Initialize: $\mathbf{Q} \leftarrow \mathbf{Q}^0$; $\mathbf{Q}^* \leftarrow \mathbf{Q}^0$; $T \leftarrow T_{\max}$.
while $T > T_{\min}$ **do**
 Obtain a random neighbour $\mathbf{Q}^{\text{new}} \leftarrow \mathbf{Q} + \Delta\mathbf{Q}$;
 if $dE \triangleq f(\mathbf{Q}) - f(\mathbf{Q}^{\text{new}}) < 0$ **then**
 $\mathbf{Q} \leftarrow \mathbf{Q}^{\text{new}}$;
 if $f(\mathbf{Q}^*) - f(\mathbf{Q}^{\text{new}}) < 0$ **then**
 $\mathbf{Q}^* \leftarrow \mathbf{Q}^{\text{new}}$;
 end
 else if $\exp\left(-\frac{dE}{T}\right) > \text{random}(0, 1)$ **then**
 $\mathbf{Q} \leftarrow \mathbf{Q}^{\text{new}}$;
 end
 Decrease the current temperature $T \leftarrow \gamma T$;
end
Output: \mathbf{Q}^* .

A. HPB-AO Algorithm

For given \mathbf{v} , the problem in (18) reduces to

$$\max_{\mathbf{Q}} f(\mathbf{Q}) \quad \text{s. t.} \quad (17d). \quad (19)$$

It can be observed from (11) to (16) that $f(\mathbf{Q})$ is highly non-convex w.r.t. \mathbf{Q} due to the involvement of sinc functions. Thus, to solve problem (19), the gradient descent algorithms are likely to be stuck in local optimum. Inspired by thermodynamic principles, we adopt the simulated annealing (SA) algorithm [14], which models the physical process of heating a material and then slowly lowering the temperature to decrease defects, so as to find a near-optimal solution.

The pseudo-code of the SA algorithm is shown in Algorithm 1. Specifically, the algorithm begins with temperature T_{\max} . At each iteration, a new point \mathbf{Q}^{new} is randomly generated, where the distance from the current point \mathbf{Q} is given by $\Delta\mathbf{Q}$. The algorithm accepts all new points that raise the objective, but also, with a certain probability, points that lower the objective. By accepting the points that lower the objective, the algorithm avoids being trapped in local maximum, and is able to explore globally for a more appealing solution. The annealing schedule systematically decreases the temperature from T to γT at each iteration, and the probability of accepting a worse solution also decreases as the algorithm proceeds. Finally, the algorithm terminates when the temperature decreases to T_{\min} and chooses the best solution \mathbf{Q}^* that explored during the annealing procedure as the algorithm output.

For given \mathbf{Q} , the problem in (18) reduces to

$$\max_{\mathbf{v}} f(\mathbf{v}) \quad \text{s. t.} \quad (17c). \quad (20)$$

This is a non-convex quadratically constrained quadratic program (QCQP) problem and can be iteratively solved by the successive convex approximation (SCA) algorithm. For given \mathbf{v}^{t-1} at the t -th iteration, we obtain from convexity that

$$f(\mathbf{v}) \geq 2\text{Re}\{(\mathbf{v}^{t-1})^H \mathbf{H} \mathbf{H}^H \mathbf{v}\} - (\mathbf{v}^{t-1})^H \mathbf{H} \mathbf{H}^H \mathbf{v}^{t-1}, \quad (21)$$

which gives an approximation of $f(\mathbf{v})$ and the equality holds at point $\mathbf{v} = \mathbf{v}^{t-1}$. By maximizing this approximation subject

Algorithm 2: SCA Algorithm

Input: Maximum iteration number I_{sca} ; relative decrease criterion ϵ_{sca} .
Initialize: \mathbf{v}^0 ; $t \leftarrow 1$.
while $t < I_{\text{sca}}$ **do**
 Update \mathbf{v} according to (22);
 if $\left| \frac{f(\mathbf{v}^t) - f(\mathbf{v}^{t-1})}{f(\mathbf{v}^{t-1})} \right| < \epsilon_{\text{sca}}$ **then**
 break;
 end
 $t \leftarrow t + 1$;
end
Output: \mathbf{v}^t .

to the constraint (17c), the closed-form solution at the t -th iteration is readily given by

$$\mathbf{v}^t = e^{J \arg(\mathbf{H} \mathbf{H}^H \mathbf{v}^{t-1})}. \quad (22)$$

Based on the above discussions, we provide the implementation details of the SCA algorithm in Algorithm 2.

In HPB-AO, \mathbf{Q} and \mathbf{v} are alternately optimized until convergence. The iteration involved may be still time-consuming. As such, we next propose a two-stage algorithm, termed HPB-Strongest-Path-Pairing (HPB-SPP), to strike a more appealing balance between complexity and performance.

B. HPB-SPP Algorithm

The two-stage algorithm is originated from the physical significance of HPB variables. In the first stage, we propose to design \mathbf{Q} that adjusts the reflection angle of the beam reflected by RIS, aiming at steering right towards the target user through the strongest paths of the BS-RIS and the RIS-user links. In the second stage, the design of \mathbf{v} is considered to align the phases of beams that reflected by each RIS. The algorithm details are specified as follows.

1) *Stage I:* For the n -th RIS, we assume that the d -th path and the k -th path are the strongest paths of \mathbf{G}_n and \mathbf{f}_n^H , respectively. Then, the gradient \mathbf{q}_n is set by letting $s_{n,k,d}^x$ and $s_{n,k,d}^y$ in (13) and (14) to be 0, which activates the strongest paths. We emphasize that this is inconsistent with the original optimization objective in problem (18). However, simulation results demonstrate a marginal performance gap compared with the result of the HPB-AO algorithm.

2) *Stage II:* For given well designed \mathbf{Q} , we consider the same problem in (20) to align the phases.

V. NUMERICAL RESULTS

In this section, we use simulation results to evaluate the proposed HPB design. The BS is equipped with $M = 8$ antennas, emitting signals with carrier wavelength $\lambda = 0.1$ m. The parameters related to RIS configuration are $\Delta = \frac{1}{2}$ and $L^2 = 900$. Without loss of generality, D_n and K_n are assumed to be the same and denoted by P . The AoAs/AoDs are assumed to be Laplacian distributed with an angular spread $\sigma_{\text{AS}} = 10^\circ$. The complex path gain $\alpha_{n,d}$ of the BS-RIS channel is circularly symmetric complex Gaussian (CSCG) distributed, i.e., $\alpha_{n,d} \sim \mathcal{CN}(0, \sigma_{n,d}^2)$, where $\sigma_{n,d}^2$ s are randomly generated

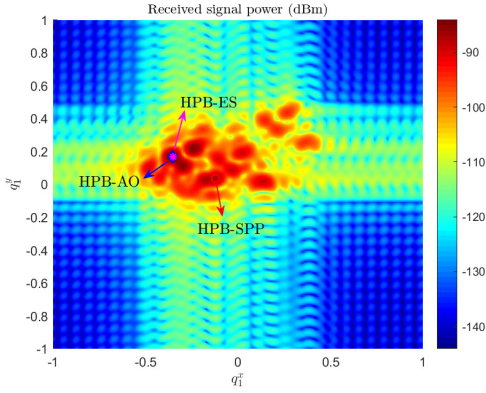


Fig. 3. Pseudo-color image of received signal power, with $P = 9$, $N = 1$.

form an exponential distribution and normalized such that $\sum_{d=1}^{D_n} \sigma_{n,d}^2 = 1$. The complex path gain $\beta_{n,k}$ of the RIS-user channel is similarly modeled and here we omit the details. Additionally, the path-loss coefficient of the cascaded channel is given by [13, Proposition 1]

$$PL_n = G_{BS} G_{RIS,n} G_{User} \frac{\Delta^2 L^4 \lambda^4}{64\pi^3 d_{1,n}^2 d_{2,n}^2}, \quad (23)$$

where $G_{BS} = 5$ dBi, $G_{RIS,n} = 5$ dBi, and $G_{User} = 0$ dBi are the antenna gains at the BS, the n -th RIS, and the user, respectively; $d_{1,n} = 50$ m and $d_{2,n} = 50$ m denote the distance from the BS to the n -th RIS, and from the n -th RIS to the user, respectively. The remaining parameters are set as follows: $p = 0.01$ W, $\sigma^2 = -100$ dBm, $T_{\max} = 10^{12}$, $T_{\min} = 10^{-24}$, $\gamma = 0.99$, $I_{\text{sca}} = 10^3$, $\epsilon_{\text{sca}} = 10^{-6}$. The experiments are carried out on a Windows x64 machine with 3.4 GHz CPU and 256 GB RAM. All the simulation curves are obtained by averaging 1000 independent channel realizations. The following PB algorithm and other comparison schemes are considered.

- **PB-SCA**: the SCA method is adopted to solve the traditional PB problem, where the closed-form expressions can be derived in each iteration.
- **HPB-ES**: for the single-RIS setup, i.e., $N = 1$, a 400×400 grid is established to exhaustively search (ES) the best solutions of q_1^x and q_1^y .
- **Random Phase Shifts**: for each channel realization, the result is averaged with 1000 randomly generated reflection coefficients.

Fig. 3 considers the single-RIS setup and plots the pseudo-color image of the received signal power w.r.t. the phase gradient components q_1^x and q_1^y , with $P = 9$. It is observed that the solution of HPB-AO almost overlaps with the global optimum of HPB obtained by exhaustive search. Moreover, as shown in the red circle label, if we select the strongest paths of the BS-RIS channel and the RIS-user channel as the incident and reflection paths directly, the solution is also reasonable good and achieves near-optimum.

In Fig. 4, the achievable rate is evaluated over the number of channel paths when $N = 1$, and over the number of RISs when $P = 9$, respectively. We see that the performance of the three HPB algorithms, namely HPB-ES, HPB-AO, and

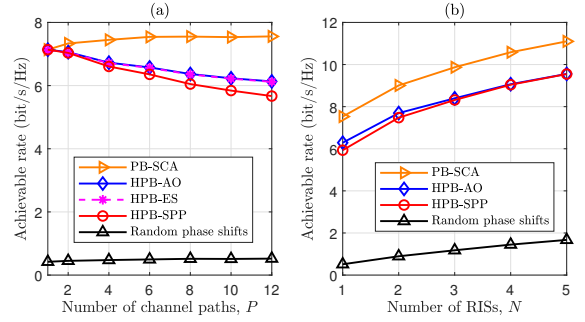


Fig. 4. Achievable rate versus (a) P , with $N = 1$; (b) N , with $P = 9$.

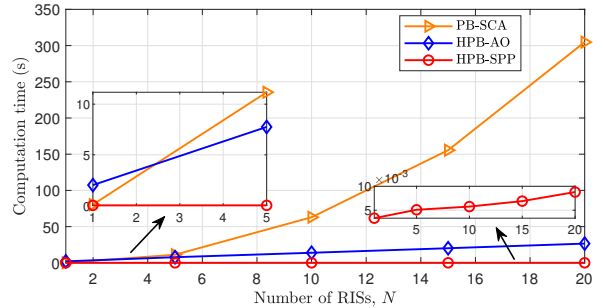


Fig. 5. Computation time versus N , with $P = 9$.

HPB-SPP, are far beyond the random phase shifts settings. Also, the performance gap between the three HPB algorithms and PB-SCA is acceptable small. When $N = 1$, HPB-AO achieves the same favourable performance as HPB-ES, while the latter incurs unaffordable complexity when N is large. Compared with HPB-SPP, as N increases, the achievable rate improvement of HPB-AO decreases since the performance of the SA procedure in HPB-AO is sensitive to the dimension of variable space.

We remark that although the PB design performs slightly better than the HPB designs, their computation complexities are quite different. It is seen from Fig. 5 that the computation time of PB-SCA rises very fast as N increases, and requires about 300 seconds to obtain a PB solution when $N = 20$. However, the computation times of both HPB-AO and HPB-SPP are low, and it is easy to meet the real-time signal processing requirement especially for the latter algorithm (less than 0.01 second even when $N = 20$).

VI. CONCLUSION

This letter proposed a new concept, i.e., HPB, for RIS reflecting coefficients design by assuming arithmetic-sequence-structured phase shifts. Experimental results evidence that the proposed solution achieves a close-to-ideal performance with significantly reduced computation complexity in PB design.

REFERENCES

- [1] C. Huang, A. Zappone, G. C. Alexandropoulos, M. Debbah, and C. Yuen, "Reconfigurable intelligent surfaces for energy efficiency in wireless communication," *IEEE Trans. Wireless Commun.*, vol. 18, no. 8, pp. 4157–4170, 2019.

- [2] Q. Wu and R. Zhang, "Intelligent reflecting surface enhanced wireless network via joint active and passive beamforming," *IEEE Trans. Wireless Commun.*, vol. 18, no. 11, pp. 5394–5409, 2019.
- [3] Z. He and X. Yuan, "Cascaded channel estimation for large intelligent metasurface assisted massive MIMO," *IEEE Wireless Commun. Lett.*, vol. 9, no. 2, pp. 210–214, 2020.
- [4] E. Basar, M. Di Renzo, J. De Rosny, M. Debbah, M. Alouini, and R. Zhang, "Wireless communications through reconfigurable intelligent surfaces," *IEEE Access*, vol. 7, pp. 116 753–116 773, 2019.
- [5] C. Pan *et al.*, "Multicell MIMO communications relying on intelligent reflecting surfaces," *IEEE Trans. Wireless Commun.*, vol. 19, no. 8, pp. 5218–5233, 2020.
- [6] H. Guo, Y. Liang, J. Chen, and E. G. Larsson, "Weighted sum-rate maximization for reconfigurable intelligent surface aided wireless networks," *IEEE Trans. Wireless Commun.*, vol. 19, no. 5, pp. 3064–3076, 2020.
- [7] P. Wang, J. Fang, X. Yuan, Z. Chen, and H. Li, "Intelligent reflecting surface-assisted millimeter wave communications: Joint active and passive precoding design," *IEEE Trans. Veh. Technol.*, pp. 1–1, 2020.
- [8] N. Yu *et al.*, "Light propagation with phase discontinuities: generalized laws of reflection and refraction," *Science*, vol. 334, no. 6054, pp. 333–337, 2011.
- [9] O. E. Ayach, S. Rajagopal, S. Abu-Surra, Z. Pi, and R. W. Heath, "Spatially sparse precoding in millimeter wave MIMO systems," *IEEE Trans. Wireless Commun.*, vol. 13, no. 3, pp. 1499–1513, 2014.
- [10] R. Schroeder, J. He, and M. Juntti, "Passive RIS vs. hybrid RIS: A comparative study on channel estimation," *arXiv:2010.06981*, 2020.
- [11] Ö. Özdogan, E. Björnson, and E. G. Larsson, "Intelligent reflecting surfaces: Physics, propagation, and pathloss modeling," *IEEE Wireless Commun. Lett.*, vol. 9, no. 5, pp. 581–585, 2019.
- [12] A. Tarable *et al.*, "Meta-surface optimization in 6G sub-THz communications," in *2020 IEEE Int. Conf. on Comm. Workshops (ICC Workshops)*. IEEE, 2020, pp. 1–6.
- [13] W. Tang *et al.*, "Wireless communications with reconfigurable intelligent surface: Path loss modeling and experimental measurement," *IEEE Trans. Wireless Commun.*, pp. 1–1, 2020.
- [14] S. Kirkpatrick, C. D. Gelatt, and M. P. Vecchi, "Optimization by simulated annealing," *Science*, vol. 220, no. 4598, pp. 671–680, 1983.